



Research Article

Design and Tensor Impedance Analysis of 4×4 Isotropic Homogeneous Metasurface-Backed Slotted Dual-Layered Bio-Superstrate-Loaded MPA

Swarnadipto Ghosh ¹, Samik Chakraborty,² Ayona Chakraborty ³, and Bhaskar Gupta³

¹Indian Institute of Space Science and Technology, Trivandrum, India

²Regent Education and Research Foundation, Kolkata, India

³Jadavpur University, Kolkata, India

Correspondence should be addressed to Swarnadipto Ghosh; swarnadipto.2000@gmail.com

Received 16 February 2024; Revised 6 April 2024; Accepted 4 May 2024; Published 18 May 2024

Academic Editor: Chow-Yen-Desmond Sim

Copyright © 2024 Swarnadipto Ghosh et al. This is an open access article distributed under the Creative Commons Attribution License, which permits unrestricted use, distribution, and reproduction in any medium, provided the original work is properly cited.

A 4×4 Isotropic Homogeneous Metasurface (IHM) backed, rectangular slotted dual-layered triband microstrip patch antenna (MPA) is proposed in this article. A detailed mathematical way to analyze the tensor surface impedance matrix (TSIM) of the proposed 4×4 IHM and slotted patch is demonstrated. The proposed IHM-backed MPA has a triband even-mode resonance at $f_{r0} = 2.45$ GHz, $2f_{r0} = 5.4$ GHz, and $4f_{r0} = 7.7$ GHz. A better and more accurate estimation of bio-superstrate loading effect for triband resonance is employed using the human skin ($\epsilon_r = 52.79$, $\sigma_s = 1.39$) and blood ($\epsilon_r = 52.8$, $\sigma_s = 1.23$) layer on the top of dual-layered metasurface-backed slotted MPA. TSIM characterization is observed for both blood- and skin layer-loaded dual-layered metasurface-backed slotted MPA. Chicken breast ($\epsilon_r = 55.2$, $\sigma_s = 1.49$, and $\tan \delta = 0.325$) with blood ($\epsilon_r = 58.2$, $\sigma_s = 2.59$, and $\tan \delta = 0.364$) is loaded onto fabricated dual-layered structure to verify numerically modeled estimation. A closed form triband, even-order resonance mode (i.e., f_{r0} , $2f_{r0}$, and $4f_{r0}$) estimation based on dielectric superstrate thickness (H_s) is numerically established using MATLAB solver. Complete measurement setup with simulated vs. measured results is compared in this article.

1. Introduction

Alteration of impedance and radiation properties of microstrip antennas with superstrate loading has been exploited extensively [1–4]. Dielectric properties of beet, beer liver, chicken, and salmon have been studied in [5] for the knowledge of their compositions and interactions with matter at various frequencies. Some work towards using single resonance frequency estimation over an antenna to determine its behavior has been already done [6–9]. Das and Mitra [10] have designed implantable antenna using thin and biocompatible substrate–superstrate layers using chicken breast slab. Metasurface-backed MPA is used to generate multiple resonance modes to improve the accuracy of estimation of dielectric loading effects. In [11], a triple-band circularly

polarized implantable patch antenna for biotelemetry applications using chicken tissue mimicking the electrical properties of human tissue has been done using a three-layer model, viz., skin, fat, and muscle, but here, the mathematical formulations for estimation of physical parameters have not been shown. Thereby, here, TSIM of a triple resonator IHM backed MPA has been used to establish a generalized empirical relation for resonance behavior based on the superstrate height. Here, chicken breast and blood have been used as superstrate for the above characterization.

In this article, a 4×4 IHM-backed slotted dual-layered triband planer microstrip patch antenna (MPA) has been numerically and analytically characterized. A complete design strategy and TSIM analysis of multilayer superstrate-loaded dual-layered IHM-backed slotted MPA has been discussed in

Section 2. Performance for each layered cases has been analyzed with adequate measurement setup in Section 3. For the variation of f_{r0} and S_{11} characterization based on ϵ_r and H_s , an empirical relationship is being modeled for multifrequency estimation and validated with available simulated and measured results in Section 4. Finally, this paper concludes with a future aspect and application note of the proposed work in Section 5.

2. Antenna Design and Tensor Impedance Matrix Analysis

Dual-layered TSIM characterization and step-by-step design strategy of the proposed 4×4 IHM-backed slotted dual-layered MPA has been demonstrated in this section. To observe the closed cavity loading effect on surface impedance ($\overline{\overline{Z_{\text{surf}}}}$), TSIM has been analyzed for bio-superstrate-loaded MPA.

2.1. Design Steps of IHM-Backed Dual-Layered MPA. Layer #1 consists a 135° rotated rectangular ($L_{\text{sl}} \times L_{\text{sw}}$) slotted MPA, having dimensions of $L_p \times L_p$ being mounted on dielectric substrate #1 ($\epsilon_r = 2.2$ and $\tan \delta = 0.0009$). In layer #2, a 4×4 planar array of isotropic meta unit cell with overall dimensions of $L_{\text{mp}} \times L_{\text{mw}}$ has been mounted on substrate #2. To realize the effect of IHM backing on slotted patch, material and dimensional ($L_s \times L_s \times H_s$) property of substrate #1 and substrate #2 has been taken similar. A PEC ground has been placed at the bottom side of substrate #2. It is shown that the proposed dual-layered MPA has been coaxially fed at L_f and W_f . Both simulated (dual and single layer) and fabricated prototypes are shown in Figure 1.

Mostly, to impose a continuous variation in both phase and amplitude of propagating wave through 4×4 IHM, the metallic metapatch of $\approx \lambda_0/15$ length is chosen with a periodicity of $\approx \lambda_0/10$. Here, λ_0 is the free space wavelength for TM_{01} mode resonance of the proposed MPA at $f_r = 2.5$ GHz. Moreover, an eigenmode solution is performed to choose the fundamental zero phase resonating frequency (f_r) with a Q-factor of 1621.54. For layer #1, a thorough parametric study of L_{sl} and L_{sw} parameter has been carried out to ensure the fundamental TM_{01} resonance mode at $f_r = 2.5$ GHz. A tight magnetic coupling between narrow slot boundary is the fundamental reason for optimizing the resonance frequency at $f_r = 2.5$ GHz.

In Figure 2, a compact measurement setup using VNA is shown with a comparison of S_{11} characteristics of simulated and fabricated structures. It is shown that the proposed dual-layered MPA can be operated at $f_{r0} = 2.45$ GHz, $\sim 2f_{r0} = 5.5$ GHz, and $\sim 4f_{r0} = 8.7$ GHz having $S_{11} \leq -18$ dB. Due to having 4×4 (i.e., even-order composition) IHM, the particular eigenvalues of IHM's decomposition matrix give even-order deterministic solution which shows similar effect for f_{r0} , $\sim 2f_{r0}$, and $\sim 4f_{r0}$ frequencies.

2.2. TSIM Analysis of Layer #1 and Layer #2 of the Proposed MPA. A complete TSIM analysis of anisotropic layer #1 and isotropic homogeneous layer #2 has been demonstrated

using floquet port analysis of Ansys HFSS and shown in Figure 3. $\overline{\overline{Z_{\text{surf}}}}$ for both layer #1 and layer #2 has been separately analyzed using two-step transverse resonance method (TSRM) by taking its equivalent transmission line model. It is seen from Figure 2 that using simulated input admittance ($\overline{\overline{Y_{\text{in}}}}$), we can extract sheet impedance ($\overline{\overline{Z_{\text{sheet}}}}$) and overall surface impedance ($\overline{\overline{Z_{\text{surf}}}}$), respectively. Using (1)-(3), the $\overline{\overline{Z_{\text{surf}}}}$ can be extracted by TSRM.

Effective guided impedance (η_1 or Z_1) = ($Z_0/\sqrt{\epsilon_r}$), guided wave vector (k_1) = $k_0\sqrt{\epsilon_r}$, and $H_s = d$ = substrate thickness can be derived to express TSRM matrix $\overline{\overline{Z_{\text{in}}}}$ at fundamental mode frequency (FOM) = 2.5 GHz.

$$\overline{\overline{Z_{\text{sheet}}}} = \overline{\overline{Y_{\text{sheet}}^{-1}}} = \begin{pmatrix} Y_{xx}^{\text{in}} - \frac{1}{jZ_1 \tan(k_1 d)} & Y_{xy}^{\text{in}} - [0] \\ Y_{yx}^{\text{in}} - [0] & Y_{yy}^{\text{in}} - \frac{1}{jZ_1 \tan(k_1 d)} \end{pmatrix}^{-1}. \quad (1)$$

Here, tensor $\overline{\overline{Y_{\text{in}}}}$ matrix can be evaluated from the simulation.

It can be said from [12] that for extracting $\overline{\overline{Z_{\text{sheet}}}}$ from $\overline{\overline{Z_{\text{in}}}}$, $\eta_0^{\text{TM}} = \eta_0$ and $\eta_1^{\text{TM}} = \eta_1$, while for the extraction of $\overline{\overline{Z_{\text{surf}}}}$ using $\overline{\overline{Z_{\text{sheet}}}}$ in (3), $\eta_0^{\text{TM}} = \eta_0(k_{z0}/k_0)$ and $\eta_1^{\text{TM}} = \eta_0(k_{z1}/k_1) = \eta_0 k_{z1}/k_0 \epsilon_r$ are being considered. Solving (2) and (3) numerically using MATLAB, $\overline{\overline{Z_{\text{surf}}}}$ can be extracted.

$$\frac{1}{Z_{\text{surf}}} = \frac{1}{Z_{\text{sheet}}} + \frac{k_0 \sqrt{\epsilon_r}}{jZ_0 k_{x1} \tan(k_{x1} d)}, \quad (2)$$

$$k_{x1} = \sqrt{k_0^2 (\epsilon_r - 1) + \left(\frac{k_0 Z_{\text{surf}}}{Z_0} \right)^2}. \quad (3)$$

Using the above-mentioned TSRM relationships, $\overline{\overline{Z_{\text{sheet}}}}$ and $\overline{\overline{Z_{\text{surf}}}}$ for both layer #1 and layer #2 have been extracted below.

$$\begin{aligned} \left(\overline{\overline{Z_{\text{sheet}}}} \right)_{\#1} &= -j \begin{pmatrix} 16.80 & -7.0 \\ -7.0 & 16.80 \end{pmatrix} \& \left(\overline{\overline{Z_{\text{sheet}}}} \right)_{\#2} &= -j \begin{pmatrix} 498 & 0.01 \\ 0.01 & 498 \end{pmatrix}, \\ \left(\overline{\overline{Z_{\text{surf}}}} \right)_{\#1} &= j \begin{pmatrix} 141.0 & 7.00 \\ 7.00 & 141.0 \end{pmatrix} \& \left(\overline{\overline{Z_{\text{surf}}}} \right)_{\#2} &= j \begin{pmatrix} 17.571 & 0.01 \\ 0.01 & 17.571 \end{pmatrix}. \end{aligned} \quad (4)$$

Diagonally slotted metallic sheet creates diagonal anisotropy, which gives the overall Z_{surf} matrix to a nondeterministic solution. Using conventional isotropic metasurface structure, the authors propose a triband periodically even-mode excited slotted MPA. Further, this even-order resonance mode excited radiating element has been numerically analyzed, and mathematical estimation is imposed for the characterization of bio-superstrate loading effect.

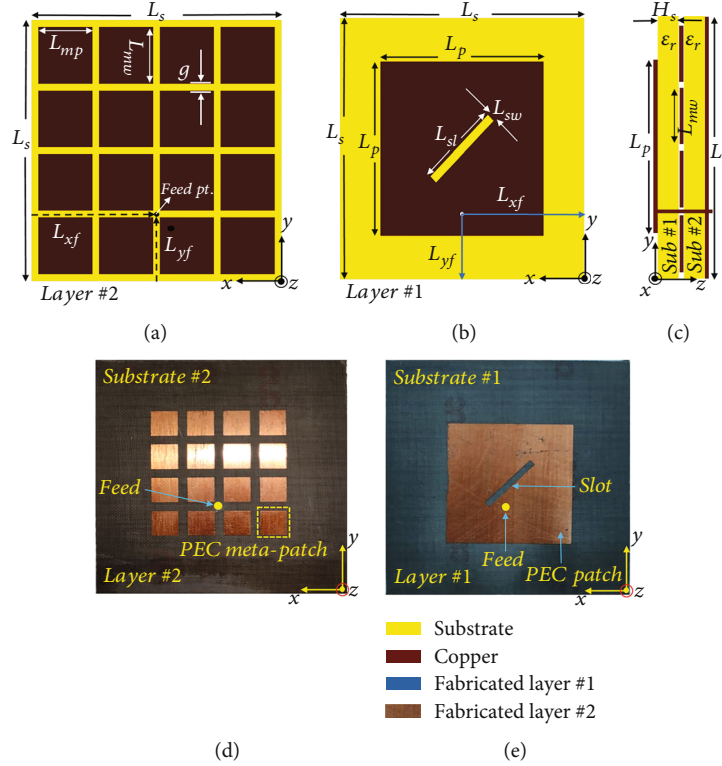


FIGURE 1: Top view of the proposed (a) layer #1 and (b) layer #2; (c) side view of complete dual-layered antenna; fabricated prototype of (d) layer #1 and (e) layer #2. Dimensions (in mm): $L_s = 40$, $L_{mp} = L_{mw} = 8$, $g = 2.66$, $L_{xf} = 20.6$, $L_{yf} = 13.2$, $L_p = 25$, $L_{sl} = 10$, $L_{sw} = 3.5$, and $H_s = 1.575$.

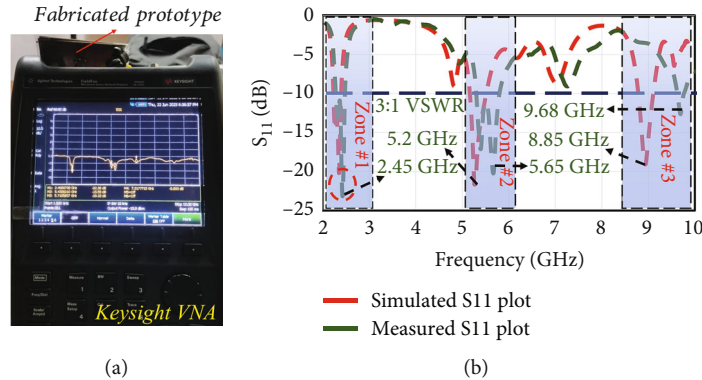


FIGURE 2: (a) Fabricated prototype measured in Keysight VNA. (b) Comparison between measured and simulated S_{11} results.

Incorporating particular dispersive phase (ϕ_{disp}) along both x and y axes, effective surface impedance (Z_{eff}) for both layer #1 and layer #2 are being determined as $j282.007 \Omega$ and $-j351.24 \Omega$, respectively, at $\theta_{k_z} = 45^\circ$. Tensor surface current distribution (\overline{J}_{surf}) is being shown for both layer #1 and layer #2 in Figure 4 to visualize the effective current density due to floquet port excitation. Using floquet excitation, the surface current distribution is observed in Figure 4 for layer #1 and layer #2 without any dielectric loading on it. Bilinear current distribution is observed at layer #1, while a unidirectional, mutually coupled orthogonal surface current is observed at Layer #2. Subwavelength metallic patches are

horizontally coupled with leaky magnetic current vectors, shown in Figure 4(b). It can be observed that due to low lossy substrate, less fringing electric current vectors are influencing the 4×4 metasurface whereas leaky magnetic current effects more due to periodically loaded metal-dielectric boundary at layer #2. Mostly, to characterize only the dual-layered metasurface-backed slotted metallic structure from impedance point of view, both sheet and surface impedance matrix are mentioned in (4). The 4×4 periodically loaded meta unit cell array (layer #2) acts as a high impedance surface and backed the slotted metallic structure (layer #1). Leaky magnetic current vectors ($M_s = -\hat{n} \times \vec{E}_t$)

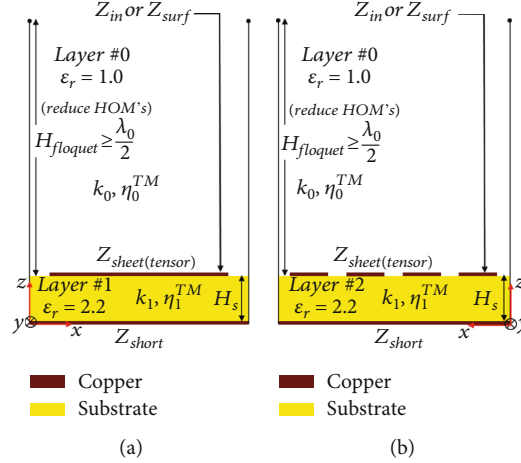


FIGURE 3: Modified modal tensor impedance analysis based on transmission line model or transverse resonance method (TSRM) for (a) slotted MPA and (b) 4×4 IHM.

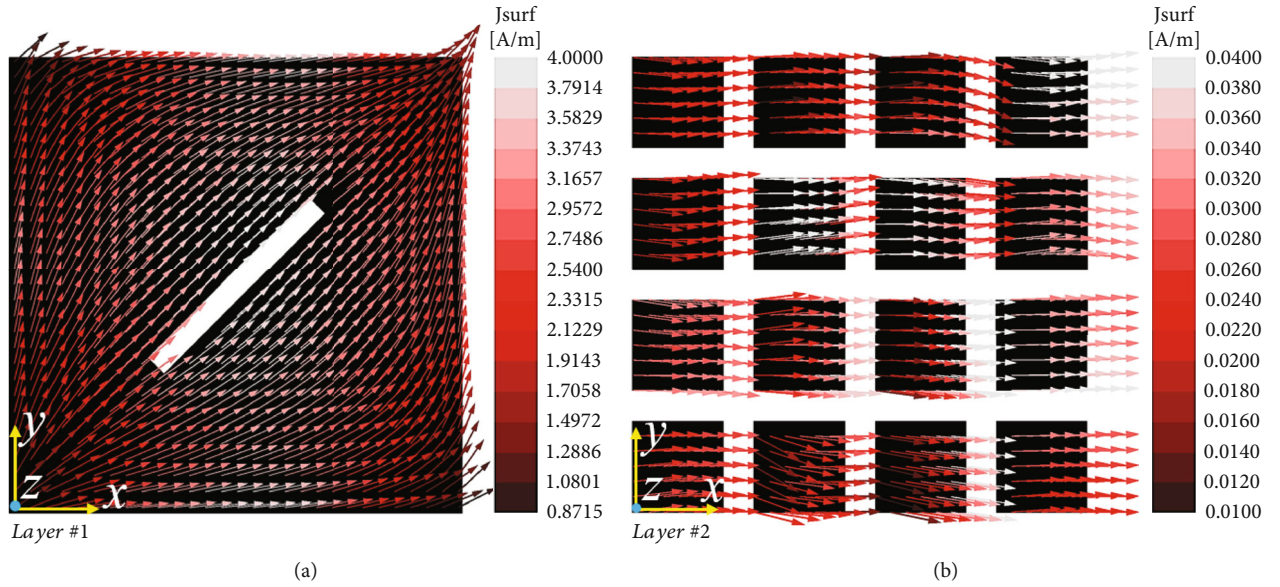


FIGURE 4: Surface current distribution on layer #1 and layer #2.

influence the overall fringing electric field components. Moreover, it can be seen from (4) that isotropic, homogeneous metasurface (IHM) exhibits a scalar impedance matrix which directly effects the resonance modes (i.e., generating even-order resonance modes) of overall dual-layered structure.

2.3. Multilayer TSIM Analysis of Superstrate-Loaded MPA. To analyze the TSRM analysis of multilayer superstrate-loaded proposed MPA, $\overline{\overline{Z}}_{\text{sheet}}$ matrix can be modeled as

$$\overline{\overline{Z}}_{\text{sheet}} = \overline{\overline{Y}}_{\text{sheet}}^{-1} = \begin{pmatrix} Y_{xx}^{\text{in, modified}} & Y_{xy}^{\text{in}} \\ Y_{yx}^{\text{in}} & Y_{yy}^{\text{in, modified}} \end{pmatrix}^{-1}. \quad (5)$$

Here, Y_{xx}^{in} and Y_{yy}^{in} can be derived as (6)

$$Y_{xx \text{ or } yy}^{\text{in}} = Y^{\text{in}} - \sum_{n=1}^{N_m} \frac{1}{jZ_{n1} \tan(k_{n1} d_n)} - Y_{\text{dual}}^{\text{in}}. \quad (6)$$

Here, N_m is the no. of stacked dielectric superstrate layer on the proposed IHM-backed MPA, Z_{n1} is the effective impedance, and d_n is the dielectric thickness for n^{th} layered superstrate loading on the proposed MPA. The mentioned $Y_{\text{dual}}^{\text{in}}$ can be expressed as a tensor admittance matrix for the proposed 4×4 IHM-backed slotted dual-layered MPA. Input tensor admittance matrix ($Y_{\text{dual}}^{\text{in}}$) can be analytically demonstrated and calculated using $Y_{\text{dual}}^{\text{in}} = (Z_{\text{dual}}^{\text{in}})^{-1}$, where $Z_{\text{dual}}^{\text{in}}$ can be determined for dual-layered metasurface-backed structure using MOM in [13]. While calculating the

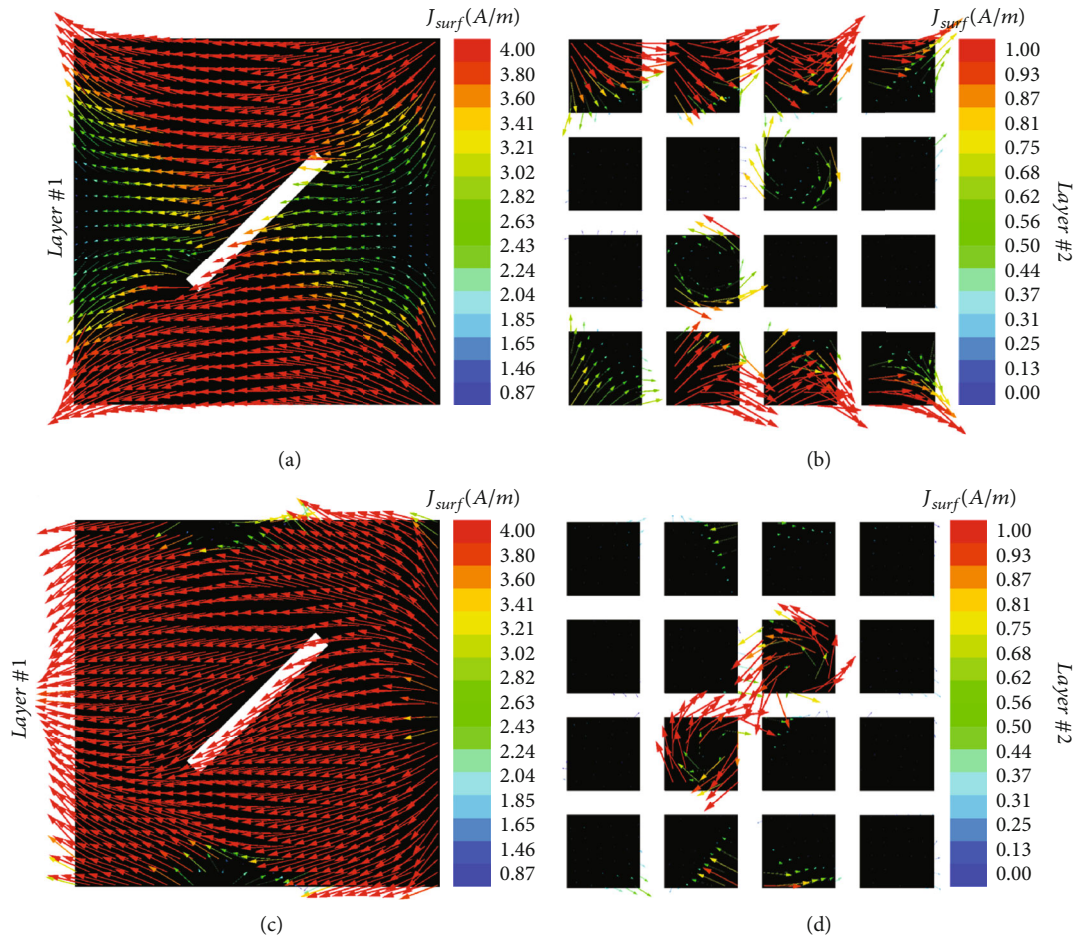


FIGURE 5: Surface current distribution of layer #1 and layer #2 for the (a, b) skin and (c, d) skin- and blood-loaded metasurface-backed slotted MPA.

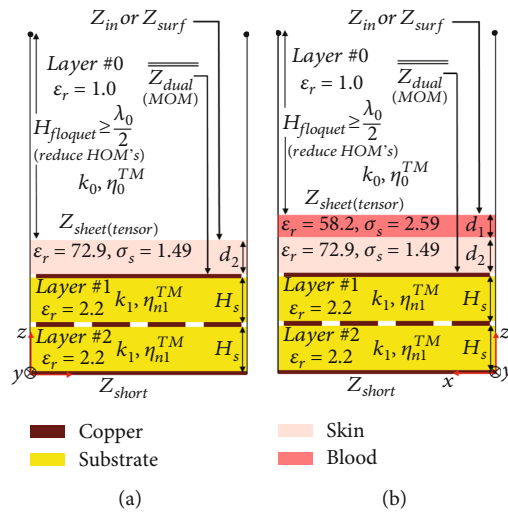


FIGURE 6: Modified modal tensor impedance analysis based on transmission line model or transverse resonance method (TSRM) for (a) slotted MPA and (b) 4×4 IHM.

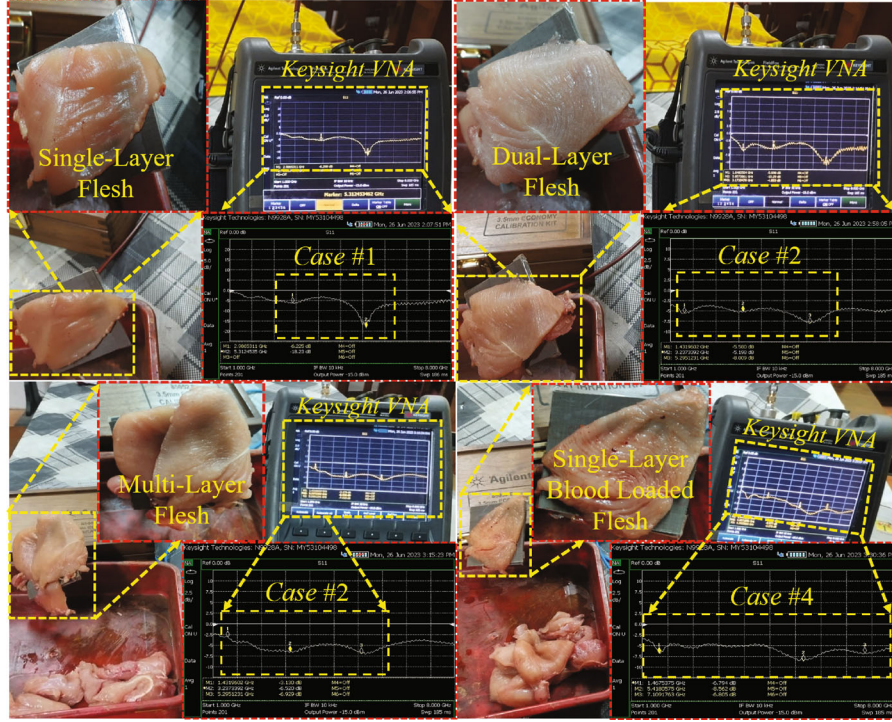


FIGURE 7: Experimented cases #1-#4 based on single-, dual-, and multilayered chicken flesh with and without blood-loaded IHM-backed MPA.

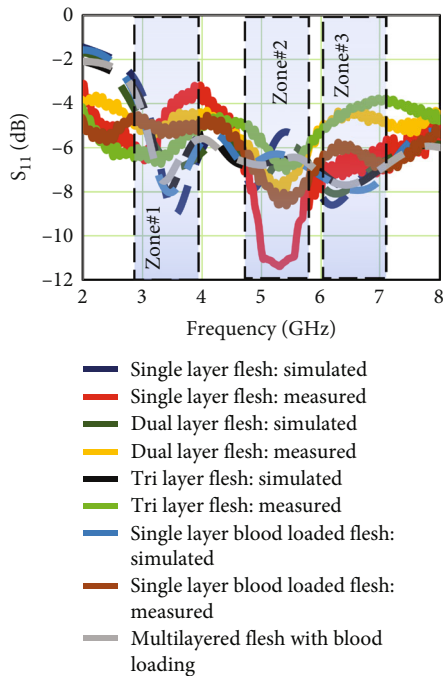


FIGURE 8: Simulated and measured S_{11} characterization based on all mentioned cases #1-#4 in Figure 7.

multilayer stacked $\overline{\overline{Z}}_{\text{surf}}$ analytically using the TSRM, it is formulated as (6).

$$\frac{1}{Z_{\text{surf}}} = \frac{1}{Z_{\text{sheet}}} - \sum_{n=1}^{N_m} \frac{k_0 \sqrt{\epsilon_{nr}}}{jZ_0 k_{x1n} \tan(k_{x1n} d_n)} - \frac{1}{Z_{\text{sheet}}^{\text{dual}}}. \quad (7)$$

Similarly, $Z_{\text{sheet}}^{\text{dual}}$ can be numerically extracted using impedance boundary condition (IBC) and method of moments (MOM) [13] for dual-layered metasurface-backed structure. Using the above-mentioned TSRM relationships, $\overline{\overline{Z}}_{\text{sheet}}$ and $\overline{\overline{Z}}_{\text{surf}}$ have been extracted while both ≈ 1 mm thick blood ($\epsilon_r = 52.8$, $\sigma_s = 1.23$) and skin ($\epsilon_r = 52.79$, $\sigma_s = 1.39$) bio-superstrate have been sequentially loaded on the proposed slotted IHM-backed dual-layered MPA. Using MATLAB, a transcendental equation has been formulated based on (7) and $Z_{\text{sheet}}^{\text{dual}}$ is being linked from MOM solution to analyze $\overline{\overline{Z}}_{\text{surf}}$.

$$\left(\overline{\overline{Z}}_{\text{sheet}}\right)_{\text{sk}} = j \begin{pmatrix} 111.3 & -222.4 \\ -222.4 & 111.3 \end{pmatrix} \& \left(\overline{\overline{Z}}_{\text{sheet}}\right)_{\text{bl}} = j \begin{pmatrix} -45.4 & 0.01 \\ 0.01 & -45.4 \end{pmatrix},$$

$$\left(\overline{\overline{Z}}_{\text{surf}}\right)_{\text{sk}} = j \begin{pmatrix} 14.74 & -222.4 \\ -222.4 & 14.74 \end{pmatrix} \& \left(\overline{\overline{Z}}_{\text{surf}}\right)_{\text{bl}} = j \begin{pmatrix} 26.98 & 0.01 \\ 0.01 & 26.98 \end{pmatrix}. \quad (8)$$

Using unidirectional circuit elements, the dual-layered as well as dielectric-layered structured architecture is costly to manufacture and analyze. An equivalent sheet impedance

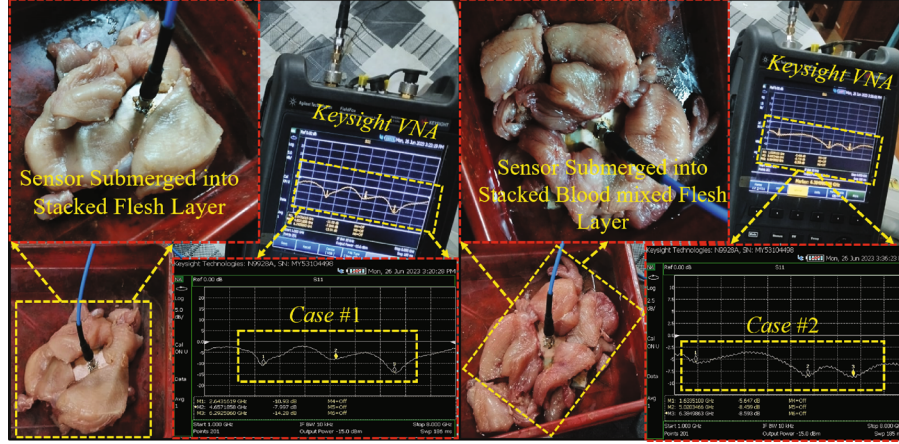


FIGURE 9: Experimented cases #1-#2 based on with and without blood-coated chicken flesh-wrapped IIM-backed slotted MPA.

TABLE 1: Polynomial coefficient ($P_{mn}^{f_{r0}}$) of low frequency (f_{r0}) mapping.

n	m				
	0	1	2	3	4
0	0.1618	-7.464	5.341	-1.174	0.0895
1	7.748	-1.305	-0.2635	0.0235	0
2	-2.347	0.6093	0.0110	0	0
3	0.1858	-0.0677	0	0	0
4	0.0007	0	0	0	0

TABLE 2: Polynomial coefficient ($P_{mn}^{f_{r0}}$) of mid frequency ($\sim 2f_{r0}$) mapping.

n	m				
	0	1	2	3	4
0	0.908	-9.47	7.812	-1.705	0.1232
1	13.38	-4.828	-0.2341	0.0596	0
2	-4.062	1.756	-0.0533	0	0
3	0.2493	-0.1437	0	0	0
4	0.01817	0	0	0	0

TABLE 3: Polynomial coefficient ($P_{mn}^{f_{r0}}$) of high frequency ($\sim 4f_{r0}$) mapping.

n	m				
	0	1	2	3	4
0	1.011	-1.806	3.684	-0.842	0.05508
1	12.33	-6.287	0.3103	0.02983	0
2	-3.762	1.728	-0.0933	0	0
3	0.337	-0.1152	0	0	0
4	-0.00325	0	0	0	0

matrix for layer #1 and layer #2 is evaluated in the place of lumped circuit model. Tensor surface impedance matrix (Z_{surf}) analysis for dual- or multilayered dielectric-loaded metasurface-backed slotted MPA is derived in (6) and (7). As similar as Section 2.2, tensor current vector distribution ($\overline{J}_{\text{surf}}$) on both superstrate-loaded surfaces is being shown in Figure 5 to visualize the surface current density due to floquet port. Effective surface impedance (Z_{eff}) for both superstrate-loaded MPA are being determined as $-j415.38\Omega$ and $j53.97\Omega$, respectively, at $\theta_{k_z} = 45^\circ$.

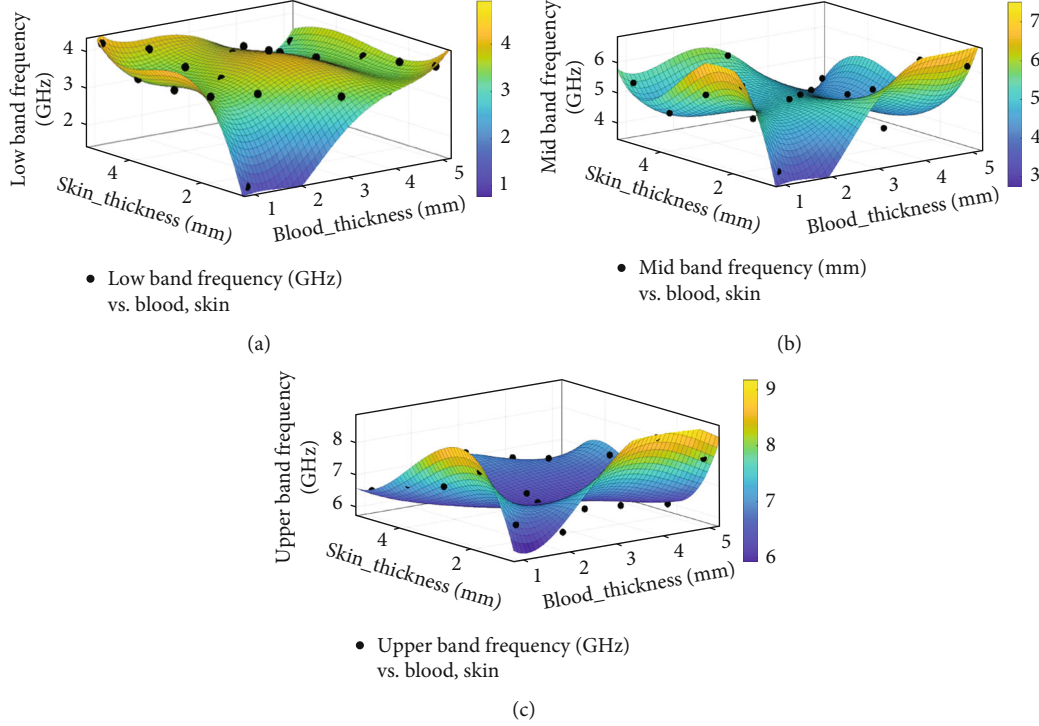
After bio-superstrate loading onto the proposed dual-layered metasurface-backed structure, a drastic change in current distribution is observed into Figure 5. Using floquet excitation method, the proposed dual-layered structure is loaded with skin and blood dielectric layer in Figure 6. Bilinear surface current is distributed towards the radiating edges where the nonradiating edges are having low current density in each side, shown in Figures 5(a) and 5(c). After bio-superstrate loading, dominant leaky magnetic current vectors are coupled at the edges and center as well (mentioned in Figures 5(b) and 5(d)) which is completely depends on the effective tensor surface impedance matrix, shown in (7). As can be seen from (7), the single-layered (i.e., only skin) bio-superstrate loading improves the off-diagonal Z_{surf} components (Z_{xy} and Z_{yx}) where dual-layered (i.e., skin and blood layered) bio-superstrate degrades the Z_{xy} and Z_{yx} components. It causes the high current density towards the edge and centre region for single and dual, bio-superstrate-loaded layer #1 and layer #2 portions.

3. Simulated and Measured Results for Bio-Superstrate-Loaded Proposed MPA

To validate the tensor impedance characterization for stacked superstrate loading upon IHM-backed dual-layered MPA, chicken flesh ($\epsilon_r = 55.2$, $\sigma_s = 1.49\text{ S/m}$, and $\tan \delta = 0.349$) with blood ($\epsilon_r = 58.2$, $\sigma_s = 2.59\text{ S/m}$, and $\tan \delta = 0.364$) has been superstrated. In Figure 7, it is shown that single, dual, and multilayer chicken flesh (having thickness (h_{flesh}) of $\approx 1.5\text{ mm/layer}$) with blood layer (with thickness (h_{blood}) of

TABLE 4: Mathematical modelling validation with simulated and measured results.

Analysis method	Output basis (f_r)		
	f_{r0}	$\sim 2f_{r0}$	$\sim 4f_{r0}$
Simulated result	3.3 GHz	5.25 GHz	6.95 GHz
Measured result	3.05 GHz	5.45 GHz	6.65 GHz
Empirically modeled result	3.2 GHz	5.3 GHz	6.74 GHz

FIGURE 10: 3D curvilinear plots at (a) f_{r0} , (b) $2f_{r0}$, and (c) $4f_{r0}$.

≈ 1 mm/layer) has been loaded on fabricated prototype to observe the S_{11} and resonance characteristics. In this work, a detailed study of antenna characteristics is performed with bio-superstrate loading. As the ultimate focus of this work is to propose the triband resonance frequency estimation for bio-superstrate loading, the practical implementation of this work is justified. Some wearable, implantable antenna or sensor applications require this numerical estimation to characterize the transmitter or sensing module. It is seen from Figure 6 that due to having high lossy water molecules ($\epsilon_r = 81$) and its conducting effect into chicken fleshes, sinusoidal ripples occurred in measured S_{11} responses. A high lossy dielectric loading and measurement tolerance emphasize the poor port impedance (S_{11} (dB)) matching with continuous ripples, though the measured S_{11} (dB) curves show the required pattern as simulated ones. Variation in S_{11} (dB) characteristics for each superstrate loading has been measured using Keysight VNA, shown in Figure 8.

Figure 9 illustrates that fabricated IIM-backed slotted MPA has been completely drenched into multilayered chicken fleshes, covered with thin blood layers. A complete measurement setup and S_{11} characterization has been deter-

mined in Figure 9 for both with and without blood (≈ 1.2 mm)-coated multilayered chicken flesh (≈ 3 mm)-wrapped IIM-backed slotted MPA.

4. Numerical Modelling for Performance Characterization of the Proposed IIM-Backed MPA

It is seen from Section 2 that the proposed IIM-backed slotted MPA exhibits triband resonance (i.e., $f_{r0} = 2.45$ GHz, $\sim 2f_{r0} = 5.5$ GHz, and $\sim 4f_{r0} = 8.7$ GHz). After the superstrate loading at near field of the proposed IIM-backed slotted MPA, it is obvious that each resonance frequency will realize a sustainable variation of f_{r0} and corresponding S_{11} . Using numerical curve fitting analysis, a multivariate or jointly correlated nonlinear polynomial relationship has been established for f_{r0} , $\sim 2f_{r0}$, and $\sim 4f_{r0}$ frequencies.

$$\text{Frequency}_{nf_{r0}} = \sum_{m=0}^N \sum_{n=0}^N P_{mn}^{nf_{r0}} x^n y^m. \quad (9)$$

Nonlinear regression technique such as goodness of fit method has been employed in (7) to emphasize a curve fitting jointly distributed or multivariate polynomial relationship between resonance behavior vs. dielectric superstrate height (i.e., both *blood* and *skin* layer) variations. Equivalent polynomial coefficient (P_{mn}^{f,r_0}) matrix for each numerical modelling is being displayed in Tables 1–3. To validate the numerical prediction efficiency of proposed empirical modelling, a validation has been performed between simulated, measured, and numerically modeled data by taking $h_{\text{skin}} = 1.5 \text{ mm}$ and $h_{\text{blood}} = 1 \text{ mm}$ in Table 4.

Based on (7), the nonlinear characterization of f_{r_0} , $\sim 2f_{r_0}$, and $\sim 4f_{r_0}$ upon h_{flesh} and h_{blood} has been graphically visualized through equivalent 3D curvilinear plots in Figure 9, respectively. It is seen from Figures 10(a)–10(c) that ≤ 0.5 offsetted curvilinear surface is being formed for f_{r_0} , $\sim 2f_{r_0}$, and $\sim 4f_{r_0}$.

5. Conclusion

A complete TSIM analysis for the proposed IIM-backed slotted MPA with bio-superstrate loading is being performed to characterize the scalar and tensor $\overline{\overline{Z}}_{\text{surf}}$ behavior. A triband frequency shifting estimation and prediction is performed to acquire more bio-superstrate loading effect on f_r and S_{11} from the proposed empirically modeled multivariate polynomial relationship. Multivariate modelling satisfies the accuracy and resonance frequency (f_r) prediction efficiency. To give sufficient validation of numerical modelling, comparative study between simulated, measured, and empirically modeled results for each f_r is shown. On-body simulation and adequate measurement is performed to validate the proposed concept.

Data Availability

The data is available within the article.

Conflicts of Interest

The authors declare that they have no conflicts of interest.

References

- [1] J.-S. Row and K.-L. Wong, "Resonance in a superstrate-loaded rectangular microstrip structure," *IEEE Transactions on Microwave Theory and Techniques*, vol. 41, no. 8, pp. 1349–1355, 1993.
- [2] D. Krishna, M. Gopikrishna, C. K. Aanandan, P. Mohanan, and K. Vasudevan, "Compact dual band slot loaded circular microstrip antenna with a superstrate," *Progress In Electromagnetics Research*, vol. 83, pp. 245–255, 2008.
- [3] S. K. Patel, C. Argyropoulos, and Y. P. Kosta, "Broadband compact microstrip patch antenna design loaded by multiple split ring resonator superstrate and substrate," *Waves in Random and Complex Media*, vol. 27, no. 1, pp. 92–102, 2017.
- [4] J. Guo, F. Liu, L. Zhao, G.-L. Huang, W. Lin, and Y. Yin, "Partial reflective decoupling superstrate for dual-polarized antennas application considering power combining effects," *IEEE Transactions on Antennas and Propagation*, vol. 70, no. 10, pp. 9855–9860, 2022.
- [5] V. N. Tran and S. S. Stuchly, "Dielectric properties of beet, beer liver, chicken and salmon at frequencies from 100 to 2500 MHz," *Journal of Microwave Power and Electromagnetic Energy*, vol. 22, no. 1, pp. 29–33, 1987.
- [6] S. Sukhija and R. K. Sarin, "A U-shaped meandered slot antenna for biomedical applications," *Progress In Electromagnetics Research M*, vol. 62, pp. 65–77, 2017.
- [7] K. C. Perumalla and P. Muthusamy, "Inductive and capacitive loaded miniaturized implantable patch antenna with circular polarization for bio-medical applications," *International Journal of RF and Microwave Computer-Aided Engineering*, vol. 32, no. 8, Article ID e23220, 2022.
- [8] W. Cui, R. Liu, L. Wang, M. Wang, H. Zheng, and E. Li, "Design of wideband implantable antenna for wireless capsule endoscope system," *IEEE Antennas and Wireless Propagation Letters*, vol. 18, no. 12, pp. 2706–2710, 2019.
- [9] A. Valanarasi and R. Dhanasekaran, "Optimum band ϵ shaped miniature implantable antennas for telemetry applications," *IEEE Transactions on Antennas and Propagation*, vol. 69, no. 1, pp. 55–63, 2021.
- [10] S. Das and D. Mitra, "A compact wideband flexible implantable slot antenna design with enhanced gain," *IEEE Transactions on Antennas and Propagation*, vol. 66, no. 8, pp. 4309–4314, 2018.
- [11] Y. A. Kamel, H. A. Mohamed, H. ELsadek, and H. M. ELhennawy, "Miniaturized triple-band circular-polarized implantable patch antenna for bio-telemetry applications," *IEEE Antennas and Wireless Propagation Letters*, vol. 22, no. 1, pp. 74–78, 2023.
- [12] J. Budhu and A. Grbic, "Perfectly reflecting metasurface reflectarrays: mutual coupling modeling between unique elements through homogenization," *IEEE Transactions on Antennas and Propagation*, vol. 69, no. 1, pp. 122–134, 2021.
- [13] J. Budhu, N. Ventresca, and A. Grbic, "Unit cell design for aperiodic metasurfaces," *IEEE Transactions on Antennas and Propagation*, vol. 71, no. 9, pp. 7387–7394, 2023.